

Phase Field Crystal Model for Magneto-Elasticity in Isotropic Ferromagnetic Solids

Niloufar Faghihi,^{1,2} Nikolas Provatas,² K. R. Elder,³ Martin Grant,² and Mikko Karttunen^{1,4}

¹*Department of Applied Mathematics, The University of Western Ontario,
1151 Richmond St. N., London, Ontario, Canada N6A 5B7*

²*Department of Physics, McGill University, 3600 rue University, Montréal, Québec, Canada H3A 2T8*

³*Department of Physics, Oakland University, Rochester, Michigan 48309, USA*

⁴*Department of Chemistry & Waterloo Institute for Nanotechnology,
University of Waterloo, 200 University Avenue West, Waterloo, Ontario, Canada N2L 3G1*

(Dated: November 8, 2018)

A new isotropic magneto-elastic phase field crystal (PFC) model to study the relation between morphological structure and magnetic properties of pure ferromagnetic solids is introduced. Analytic calculations were used to determine the phase diagram and obtain the relationship between elastic strains and magnetization. Time dependent numerical simulations were used to demonstrate the effect of grain boundaries on the formation of magnetic domains. It was shown that the grain boundaries act as nucleating sites for domains of reverse magnetization. Finally, we derive a relation for coercivity versus grain mis-orientation in the isotropic limit.

I. INTRODUCTION

The physical properties of materials and their functions are often influenced by their microstructures [1–3]. This holds true in magnetic materials where for example, the magnetic coercivity, remanence and magnetic saturation are known to be a strong function of grain size in polycrystalline materials. For applications it often useful to be able to tailor specific magnetic properties. For example in applications such as in magnetic data storage devices, sensors, motors, generators, transformers [4] it desirable to have soft magnetic materials which have high large saturation and remanent magnetization and low coercivity. These properties make them suitable for electronic devices for which a quick change of magnetization with minimum energy loss per cycle is required. Thus it is very important to understand the detailed and complex relationship between microstructures and magnetization.

Anisotropy is one of the key properties of magnetic materials. To reverse the direction of a magnetic domain, a magnetic anisotropy energy barrier must be overcome such that the magnetic moments have enough energy to deviate from the easy axis of magnetization. The other factor that determines coercivity is the local morphology of the material. For example, grain boundaries and other defects can modify the barrier for formation of a magnetic domain [5–7]. Another example is a local composition variation: a secondary soft magnetic phase could affect the initiation of magnetization reversal. Finally, the exchange interaction and magnetic dipole interactions also influence coercivity. These interactions establish collective alignment of magnetic moments which facilitates the formation of the magnetic domains [5, 8].

Understanding the relation of magnetic microstructure to crystalline microstructure can be useful for designing materials with desired magnetic properties. This is particularly true of nanocrystalline materials with grain sizes on the order of a few tens of nanometers, where grain size and magnetic correlation lengths are compa-

table. The relative magnitude of these length scales can alter the mechanism of magnetic domain formation to be controlled either by a long-range cooperative magnetic behaviour or by a local ordering. This gives rise to a relatively broad range of coercivity values attainable in nanocrystalline magnetic materials [9] and opens up new opportunities to develop ultra-high-density magnetic storage devices [10]. Understanding the physics of these systems, however, requires a robust modeling formalism that is capable of describing magneto-elastic interactions in the presence of crystalline defects and microstructural processes that evolve on diffusive time scales.

One of the first studies of the effect of crystallographic structure on the magnetic properties was by Harris *et al.* [11]. They suggested a simple Hamiltonian to describe magnetism in amorphous materials with random anisotropy. Later, this model was developed to study amorphous materials in which the magnetic correlation length spans many length scales with different anisotropy directions [12, 13]: For small grains the magnetic correlation length is larger than the grain size, the effective anisotropy is suppressed by the exchange interaction within a domain. In such materials the coercivity, H_c and the grain size, D , are related as *i.e.*, $H_c \sim D^6$. In contrast, when the grain size is larger than the magnetic correlation length, the magnetization is controlled by domain wall pinning at the grain boundaries and $H_c \sim 1/D$ [14, 15]. This simple model has formed the basis of most theories on magnetic hardness in nano-crystalline magnetic materials [16], and its predictions were confirmed by experiments [17–19].

The relationship between grain size and hysteresis continues to be the subject of numerous investigations in the field of micromagnetism [7, 10, 20, 21]. Most approaches have been based on minimization of Hamiltonians that contain terms for anisotropy, exchange, magneto-elastic and demagnetizing energies [6]. These Hamiltonians tend to be rather complex and can be solved for minimum energy configurations only in simple geometries and under certain simplifications, most of which do not adequately

reflect the complex microstructure of a material.

Magnetization has recently been coupled to phase field order parameters to describe different crystal variants or phases. Magneto-phase field free energies are then used to derive dynamical equations of microstructure evolution in the presence of magnetic field in [22–24]. The advantage of these models is that the interface between the crystalline phases emerges naturally in the dynamics of the field equations. Furthermore, in this approach the free energy is developed in terms of the coarse-grained order parameters in space and time which makes it possible to reach the diffusive time scales and the length scales necessary to study the microstructure evolution in the presence of an external magnetic field. The main drawback of traditional phase field approaches is that they lack direct coupling to plastic and elastic effects emergent from the atomic structure of crystalline phases. Information about the crystallographic structure of material typically enters through effective parameters controlling the anisotropy, exchange stiffness or the boundary conditions. Moreover, no continuum phase field type model to date incorporates the elastic and kinetic effects of topological defects.

This work introduces a new phase field crystal (PFC) model that captures the basic physics of magneto-crystalline interactions for isotropic ferromagnetic solids. The PFC approach [25, 26] is a continuum method that has been shown to capture the essential physics of atomic-scale elastic and plastic effects that accompany diffusive phase transformations, such as solidification, dislocation kinetics, solid state precipitation and epitaxial growth [3, 27–34]. This work expands the approach by coupling the PFC density with magnetization to generate a ferromagnetic solid below a density-dependent Curie temperature. The equilibrium properties of the model are first examined, followed by a single-mode derivation of the model’s magnetostriction properties. Simple dissipative dynamics are used to qualitatively illustrate coercivity to grain and domain size. Finally, a relation for the coercivity versus low angle grain boundary mis-orientation is derived.

II. MODEL DESCRIPTION

We construct a dimensionless free energy that couples three dimensionless fields, *i.e.*, the number density $n(\mathbf{x})$, the magnetization vector $\mathbf{m}(\mathbf{x})$ and the magnetic field \mathbf{B} , according to

$$\begin{aligned} \frac{\Delta F}{k_B T V \bar{\rho}} = \int d\mathbf{r} \left\{ n \left(\Delta B + B_s (1 + \nabla^2)^2 \right) \frac{n}{2} - t \frac{n^3}{3} + v \frac{n^4}{4} \right. \\ \left. + \omega \left[\frac{W_0^2}{2} |\nabla \mathbf{m}|^2 + (r_c - \beta n^2) \frac{|\mathbf{m}|^2}{2} + \gamma \frac{|\mathbf{m}|^4}{4} \right. \right. \\ \left. \left. - \frac{\alpha}{2} (\mathbf{m} \cdot \nabla n)^2 - \mathbf{m} \cdot \mathbf{B} + \frac{|\mathbf{B}|^2}{2} \right] \right\}. \quad (1) \end{aligned}$$

The dimensionless number density field is defined as $n(\mathbf{x}) \equiv (\rho(\mathbf{x}) - \bar{\rho})/\bar{\rho}$, where $\bar{\rho}$ is a reference constant density, taken to be the density of the liquid at coexistence [35]. The parameter $\omega \equiv B_0^2/(\mu_0 k_B T \bar{\rho})$ and B_0 is a reference magnetic field. The parameter k_B is the Boltzmann constant and V is the volume of the unit cell.

The first line in Eq. 1 is the usual phase field crystal (PFC) free energy [25, 26], where B_s , t , v and ΔB are dimensionless parameters related to physical properties of the material. Using the classical density functional theory of freezing (CDFT) it has been shown that B_s is related to the bulk modulus of the solid [27]. In the same framework, the bulk parameters $t = 1/2$ and $v = 1/3$ are approximated by expanding the free energy of the ideal gas about a reference density [29, 30]. In the PFC model the transition from liquid to solid occurs when ΔB changes. Decreasing ΔB is equivalent to decreasing temperature or increasing the average density of the system [35]. Space has been rescaled in terms of the lattice constant $a = 2\pi/q_o$.

The second line of the free energy approximates the magnetic free energy through a Ginzburg-Landau (GL) expansion, which accounts for a ferromagnetic phase transition [36] through $(r_c - \beta n^2)$, a factor that implicitly depends on temperature through n . This term defines the Curie temperatures. The parameters r_c and β are chosen such that the Curie temperature lies below the liquid/solid coexistence lines in the phase diagram [37–39]. The parameter W_0 sets the scale of the magnetic correlation length (in units of the lattice constant). The parameter γ is related to the saturation magnetization and the magnetic susceptibility. The term, $-\alpha/2(\mathbf{m} \cdot \nabla n)^2$ is introduced in this work as the lowest order coupling of magnetization to the gradient of the density, giving rise to magnetostriction, with α being the magnetostrictive coefficient, a very small dimensionless quantity of order $\alpha \sim 10^{-5}$ for iron, nickel and cobalt [40].

The last two terms in Eq. 1 account for the the magnetic free energy and are associated with the magnetic dipole interactions. The total local magnetic field is denoted by $\mathbf{B} = \mathbf{B}(\mathbf{r})$, where \mathbf{B} is scaled by B_0 . It is calculated by adding the induced magnetic field and the external magnetic field, $\mathbf{B}(\mathbf{r}) = \mathbf{B}_{ind}(\mathbf{r}) + \mathbf{B}_{ext}$. The induced magnetic field is a result of magnetization current density, \mathbf{J}_M and can be expressed in terms of the magnetization, \mathbf{m} according to the dimensionless Poisson’s equation [41]

$$\nabla^2 \mathbf{A} = -\nabla \times \mathbf{m}, \quad (2)$$

where \mathbf{A} is the dimensionless vector potential and is related to the induced magnetic field via $\mathbf{B}_{ind} = \nabla \times \mathbf{A}$. The value of ω can be chosen to match the measured value for a specific ferromagnetic element. Here, for simplicity we chose $\omega = 1$. In the subsequent sections we use the following model parameters in the free energy of Eq. (1): $(B_s, t, v, \alpha, W_0, \beta, r_c, \omega, \gamma) = (0.98, 0.5, 1/3, 10^{-3}, 1, 4 \times 10^{-2}, 10^{-2}, 1, 1)$.

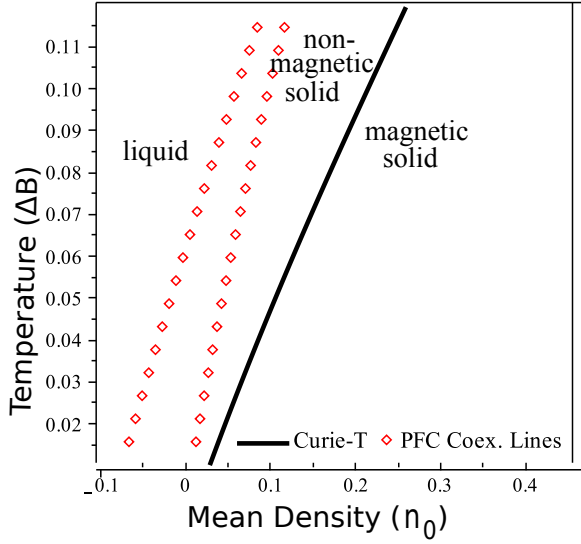


FIG. 1: Phase diagram of the Magnetic-PFC model. The dots denote the liquid-solid coexistence lines and solid line denotes the Curie line of ferromagnetic phase transition.

III. EQUILIBRIUM PROPERTIES AND MAGNETOSTRICTION

In this section, an amplitude representation of Eq. 1 is derived and then used to calculate the equilibrium phase diagram and the magnetostriction coefficients of the present model.

A. Phase Diagram

To coarse-grain the free energy, we calculated the amplitude representation of the free energy, by expanding the density in terms of the Fourier modes with spatially-dependent complex amplitudes

$$n = n_0 + \sum_j \eta_j(\mathbf{x}, t) e^{i\mathbf{q}_j \cdot \mathbf{r}} + C.C. \quad (3)$$

where n_0 represents the average density, $C.C.$ represents the complex conjugate of the expansion, $\mathbf{q}_1 = -\sqrt{3}/2\mathbf{i} - 1/2\mathbf{j}$, $\mathbf{q}_2 = \mathbf{j}$ and $\mathbf{q}_3 = \sqrt{3}/2\mathbf{i} - 1/2\mathbf{j}$ for a triangular two dimensional system and η_i are complex amplitudes corresponding to each density wave in the expansion. Equation (3) approximates the density to the lowest order harmonics of the Fourier expansion, *i.e.*, the single mode approximation. We substitute this into the free energy (and omit the energy associated with the magnetic dipole interactions in comparison to the exchange interaction) and follow the integration procedure of [42, 43], assuming that the amplitudes, $\eta_j(\mathbf{x}, t)$, vary on length scale much larger than the lattice constant. In this assumption, we can simplify the calculations by ignoring

the spatial dependence of the amplitudes over a unit cell to obtain

$$\begin{aligned} F_\eta = \int d\mathbf{r} \left\{ \left(\Delta B + B_s \right) \left(\frac{1}{2} n_0^2 + \sum_j |\eta_j|^2 \right) \right. \\ + B_s \left(- \sum_j |\eta_j|^2 + \sum_j |\mathcal{G}_j \eta_j|^2 \right) \\ - t \left(\frac{1}{3} n_0^3 + 2n_0 \sum_j |\eta_j|^2 + 2 \left(\prod_j \eta_j + \prod_j \eta_j^* \right) \right) \\ + v \left[\frac{1}{4} n_0^4 + 3n_0^2 \sum_j |\eta_j|^2 + \frac{3}{2} \sum_j |\eta_j|^4 \right. \\ + 6(|\eta_1|^2 |\eta_3|^2 + |\eta_1|^2 |\eta_2|^2 + |\eta_2|^2 |\eta_3|^2) \\ + 6n_0 \left(\prod_j \eta_j + \prod_j \eta_j^* \right) \left. \right] - \omega \alpha \sum_j |\mathcal{A}_j \eta_j|^2 \\ + \omega \left(\frac{W_0^2}{2} |\nabla^2 \mathbf{m}|^2 + \left[r_c - \beta \left(n_0^2 + 2 \sum_j |\eta_j|^2 \right) \right] \frac{|\mathbf{m}|^2}{2} \right. \\ \left. + \gamma \frac{|\mathbf{m}|^4}{4} \right) \left. \right\}, \quad (4) \end{aligned}$$

where the operators \mathcal{G}_j and \mathcal{A}_j are defined as $\mathcal{G}_j \equiv (\nabla^2 + 2i\mathbf{q}_j \cdot \nabla)$ and $\mathcal{A}_j \equiv \mathbf{m} \cdot (\nabla + i\mathbf{q}_j)$.

Following Chan and Goldenfeld [44] and others [45], we represent the complex amplitude by $\eta_j = \phi e^{i\mathbf{q}_j \cdot \mathbf{u}}$, where $\mathbf{u}(\mathbf{x})$ denotes a local elastic displacement vector. Inserting it into Eq. 4 we obtain

$$\begin{aligned} F_{\phi, U_{ij}} = \int d\mathbf{r} \left\{ \left(-\frac{t}{3} + \frac{1}{2} (\Delta B + B_s) \right) n_0^2 + \frac{v}{4} n_0^4 \right. \\ + \phi^2 (3\Delta B - 6tn_0 + 9vn_0^2) + \phi^3 (-4t + 12vn_0) + \phi^4 \left(\frac{45}{2} v \right) \\ + B_s \left[\phi^2 \left(\frac{9}{2} (U_{xx}^2 + U_{yy}^2) + 3U_{xx}U_{yy} + 6U_{xy}^2 \right) \right] \\ + \omega \left[-3\alpha\phi^2 (U_{xx}m_x^2 + U_{yy}m_y^2 + 2U_{xy}m_xm_y) \right. \\ + \left(\frac{W_0^2}{2} |\nabla \mathbf{m}|^2 + \left[r_c - \beta (n_0^2 + 6\phi^2) \right. \right. \\ \left. \left. - 3\alpha\phi^2 \right] \frac{|\mathbf{m}|^2}{2} + \gamma \frac{|\mathbf{m}|^4}{4} \right) \left. \right] \left. \right\}, \quad (5) \end{aligned}$$

where U_{ij} are the strain tensor elements and ϕ is the order parameter. ϕ is non-zero in the solid phase and zero in the liquid phase. The strain tensor is defined as

$$U_{ij} \equiv \frac{1}{2} (u_{ij} + u_{ji} + \sum_k u_{ik} u_{jk}), \quad (6)$$

with $u_{ab} \equiv \partial u_a / \partial x_b$. This form of the free energy presents a continuum description of the magnetic ma-

terial's properties which has the same level of coarse-graining as those established in [46, 47]. The main difference is that complex amplitudes now allow a description of grain boundaries and dislocations.

To calculate the equilibrium states of the system, we minimize the free energy, $F_{\phi, U_{ij}}$, with respect to the strain tensor elements, U_{ij} . The resulting, minimized, free energy becomes

$$\begin{aligned}
F_{\phi} = & \int d\mathbf{r} \left\{ \omega \left(\frac{W_0^2}{2} |\nabla \mathbf{m}|^2 + (-3\alpha\phi^2 - 6\beta\phi^2 \right. \right. \\
& + r_c - \beta n_0^2) \frac{|\mathbf{m}|^2}{2} + \left. \left. \left(\gamma - \frac{9\phi^2\omega\alpha^2}{4B_s} \right) \frac{|\mathbf{m}|^4}{4} \right) \right. \\
& + (3\Delta B - 6tn_0 + 9vn_0^2)\phi^2 + (12vn_0 - 4t)\phi^3 + \frac{45}{2}v\phi^4 \\
& \left. + \left[\frac{1}{2}(B_s + \Delta B) - \frac{1}{3}t \right] n_0^2 + \frac{1}{4}vn_0^4 \right\}. \quad (7)
\end{aligned}$$

This free energy has the form of the LG free energy containing a ferromagnetic phase transition. The coefficients depend on the mean density of the system, n_0 , the crystalline order parameter (ϕ) as well as the temperature, ΔB . The dependence of magnetic phase transition on the density is a manifestation of the connection between microstructure and magnetic properties of the material.

The fact that the magnetic energy, Eq. 7, does not depend on the relative angle of the magnetization and the direction of ∇n , reveals that the model (Eq. 1) does not include anisotropy. This is due to the fact that it contains the coupling term, $\mathbf{m} \cdot \nabla n$, only up to the second order. To involve the anisotropic effects higher order terms in $\mathbf{m} \cdot \nabla n$ are required. Anisotropy will be examined in an upcoming paper.

To find the ferromagnetic transition, we minimize F_{ϕ} with respect to the magnetization $|\mathbf{m}|$, obtaining

$$m_s = 0, \pm \sqrt{\frac{-(r_c - n_0^2\beta - 6\phi^2\beta + 3\phi^2\alpha)}{\gamma - \frac{9\omega\alpha^2\phi^2}{4B_s}}} \quad (8)$$

where ϕ is the amplitude of the density field expansion in PFC model. Minimizing the magnetic PFC free energy with respect to ϕ when $|\mathbf{m}| = 0$ yields,

$$\phi_{min} = -\frac{n_0}{5} + \frac{1}{10} + \frac{1}{10} \sqrt{1 + 16n_0 - 16n_0^2 - 20\Delta B} \quad (9)$$

Thus ϕ_{min} is a function of the mean density, n_0 , and the temperature ΔB . To find the ferromagnetic transition line in the $\Delta B - n_0$ plane, we solve

$$r_c - n_0^2\beta - 6\phi^2\beta + 3\phi^2\alpha = 0 \quad (10)$$

using $\phi = \phi_{min}$ in Eq. 9. The solution gives an equation for the Curie line in terms of ΔB and average density n_0 . This line separates the phase diagram into non-magnetic and magnetic phases.

The values of r_c and β change the position of the Curie line in the phase diagram. For a realistic model which

is in accordance with the experimental data [37–39], we choose them in such a way that the curve lies below the PFC coexistence lines. This guarantees that the ferromagnetic phase appear only in the solid. If we increase r_c or decrease β , the line will shift down. The Curie line, together with the solid-liquid coexistence lines of the model, are shown in Fig. 1. The free energy is minimized by three phases: liquid, non-magnetic solid and magnetic-solid. Above the Curie line $\mathbf{m} = 0$ and the usual PFC phase diagram reproduced.

B. Magnetostriction

The term $-\alpha/2(\mathbf{m} \cdot \nabla n)^2$ is a minimal coupling that induces magnetostriction. The strain energy is given by

$$\begin{aligned}
\mathcal{F}_{m-e} = & \int d\vec{r} \left\{ B_s (9(U_{xx}^2 + U_{yy}^2) + 6U_{xx}U_{yy} + 12U_{xy}^2) \right. \\
& \left. - 3\omega\alpha\phi^2 \left(m_x^2 U_{xx} + m_y^2 U_{yy} + 2m_x m_y U_{xy} + \frac{|\mathbf{m}|^2}{2} \right) \right\}. \quad (11)
\end{aligned}$$

Minimizing the resultant free energy with respect to the strain tensor elements yields the relations for magnetically induced strain tensor as

$$U_{xx}^{min} = \frac{\alpha\omega m^2}{8B_s} (2\cos 2\theta + 1) \quad (12)$$

$$U_{yy}^{min} = -\frac{\alpha\omega m^2}{8B_s} (2\cos 2\theta - 1) \quad (13)$$

$$U_{xy}^{min} = \frac{\alpha\omega m^2}{4B_s} \sin 2\theta, \quad (14)$$

where we have assumed that the magnetization vector has an angle θ with respect to the x -axis.

To examine the influence of magnetostriction on the crystalline states numerical simulations were conducted. In this work we were mainly interested in the equilibrated states and consequently used the simplest dissipative dynamics for both fields, such that conserved (model B [48]) dynamics were used for $n(\mathbf{x})$ and non-conserved (model A [48]) dynamics for the magnetization, i.e.,

$$\frac{\partial n(\mathbf{r}, t)}{\partial t} = \nabla^2 \frac{\delta F(n, \mathbf{m})}{\delta n} \quad (15)$$

$$\frac{\partial m_i(\mathbf{r}, t)}{\partial t} = -\frac{\delta F(n, \mathbf{m})}{\delta m_i}, \quad (16)$$

where $i = x, y$ for the magnetization in x and y directions, respectively. These equations were solved in a system with periodic boundary conditions using Euler's method for the time derivative, finite difference methods for the spatial gradients [49] and a Fourier transform algorithm to solve the Poisson equation for the vector potential \mathbf{A} .

Since the magnetically induced strain is much smaller than the elastic strain that can developed in a confined solid, this simulation was performed in a system

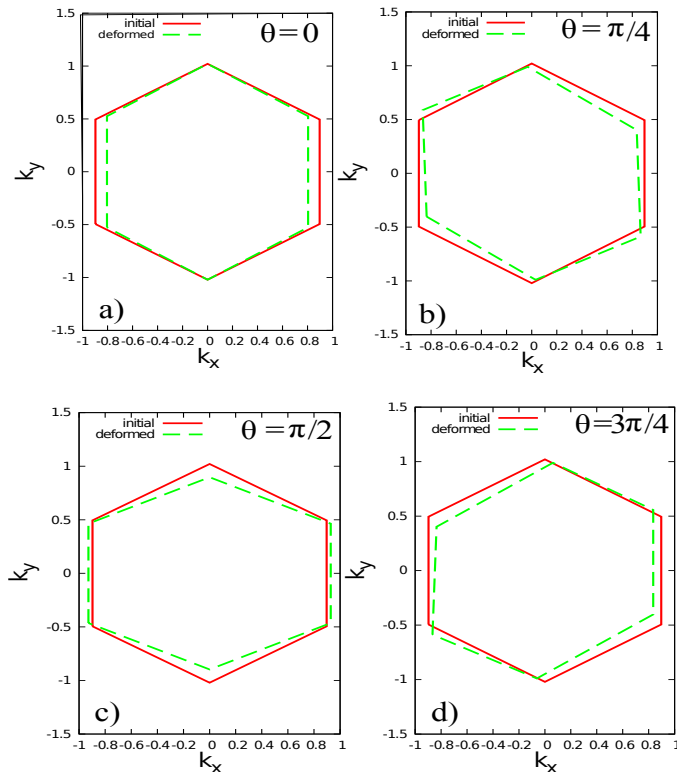


FIG. 2: The structure factor of the system of size 256×256 at coexistence. We first allow the system to equilibrate in the absence of the magnetic field and then apply a magnetic field of $|\mathbf{B}| = 9.5$ at the angle of θ with respect to the x -axis. The red hexagons show the structure factor of the initial configuration and the green deformed hexagons in (a)–(d) show the magnetically induced deformation of the hexagonal lattice at different magnetic field directions.

of coexisting liquid and solid phases. In this instance the solid can deform freely when an external magnetic field is applied. The system parameters are as follows: $(B_s, t, v, \alpha, W_0, \beta, r_c, \omega, \gamma) = (0.98, 0.5, 1/3, 10^{-3}, 1, 4 \times 10^{-2}, 10^{-2}, 1, 1)$. We chose these values so that we have a wide coexistence region for as large a value of α as possible, to make the magnetostriction large enough to be measurable. The coexistence region lies above the Curie line in the phase diagram and is paramagnetic. When an external magnetic field is applied, it will break the symmetry of the magnetic free energy, and the net magnetization of the system becomes non-zero, aligning with the external magnetic field.

An external magnetic field of $|\mathbf{B}| = 9.5$ was applied in different angles with respect to x -axis. Figure 2 shows the structure of the hexagonal solid phase for angles $\theta = 0, \pi/4, \pi/2, 3\pi/2$. In these simulations $\alpha = -0.7$ is negative which means that the sample shrinks in the direction of the applied magnetic field. The two hexagons in these figures represent the initial lattice points (red) and the deformed lattice points (green) after the

magnetic field is applied. Figure 2 clearly shows the magnetostriction effect.

IV. EFFECT OF GRAIN BOUNDARIES ON COERCIVITY

In this section we examine the influence of grain boundaries and size on the magnetic coercivity. As a baseline, we first study the mean field coercivity of a single crystal in subsection IV A and then numerically examine the influence of grain boundary misorientation and grain size in subsections IV B and IV C respectively.

A. Mean field coercivity of a single crystal

The coercivity of a single crystal in the mean field limit can be obtained by determining when the local minima of the free energy with respect to m disappears as a function of applied magnetic field \mathbf{B} . The value of \mathbf{B} at which this just occurs is the mean field coercivity. If thermal fluctuations were included a small coercivity would be obtained that would depend on how rapidly the applied field changes. To obtain the mean field coercivity we first solve $d(f_\phi - \mathbf{m} \cdot \mathbf{B})/dm = 0$, where f_ϕ is the non-gradient part of the magnetic free energy, Eq. 7, to obtain the minima of the free energy for $\mathbf{B} = B\hat{x}$. These two minima are shown in Fig. 3 for different values of external magnetic field. For $B < 0$ ($B > 0$) the negative (positive) branch has the lower free energy and positive (negative) branch is metastable. The metastable branch disappears at the mean field coercivity. As shown in Fig. 3 the coercivity is equal to $H_a = 4.7 \times 10^{-3}$. The parameters of the free energy used in this calculation and in all of the simulations of the following sections are as stated in Section II.

To examine the hysteresis behavior and magnetic coercivity, numerical simulations were conducted by solving the dynamical equations of motion, *i.e.*, Eqs. 15 and 16 using periodic boundary conditions. The external magnetic field was increased linearly from zero to a maximum of $\mathbf{B} = (0, 0.008)$ (this value was estimated using Fig. 3) and was then decreased at the same rate to complete a cycle in total time steps of 4×10^5 . The field was applied to a single crystal system and a bi-crystal system. The bi-crystal system is prepared by locating two symmetrically tilted grains, with a tilt angle of $\theta = 21.78$ degrees. With this choice for the mismatch angle, the simulation box of size 256×256 accommodates two perfect grains and the boundary effects does not disturb the energy of the grain boundary.

We calculated the mean magnetization of the two systems as a function of the applied magnetic field. The result is shown in Fig. 4. It can be seen that the coercivity is larger for a single crystal comparing to the bi-crystal system. *i.e.*, it takes a smaller external magnetic field to remove the local minimum of the free energy in the

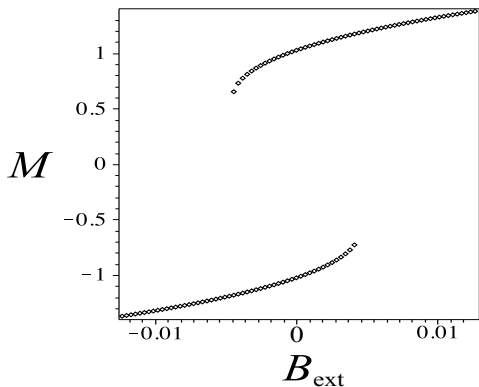


FIG. 3: The vertical axis represents the magnetization $M = m/m_s$ and the dotted lines represent the two roots of the magnetic free energy f_ϕ given in Eq. 7, corresponding to positive and negative magnetization values that minimize the free energy. When an external magnetic field is applied, the spins tend to flip to align with the magnetic field. If the magnetic field is large enough ($|\mathbf{B}| > B_a = B_a = 4.7 \times 10^{-3}$) one of the minima disappears. The value of B_a gives an estimation for the coercivity of the model with parameters $(B_s, t, v, \alpha, W_0, \beta, r_c, \omega, \gamma) = (0.98, 0.5, 1/3, 10^{-3}, 1, 4 \times 10^{-2}, 10^{-2}, 1, 1)$.

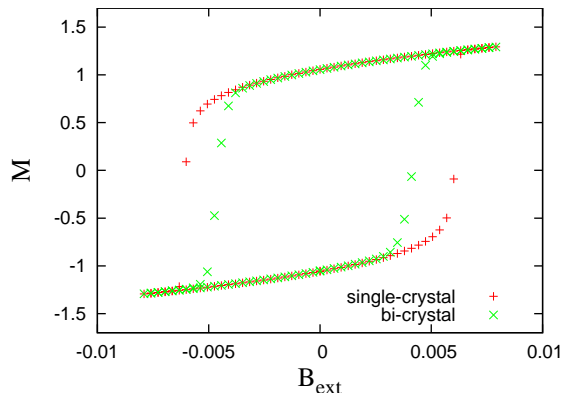


FIG. 4: Hysteresis curves for single crystal and bi-crystalline systems. The two-grain system is produced by placing two hexagonal crystal lattices that are rotated symmetrically with respect to each other. To produce the perfect fit inside the boxes, the lattice spacing was chosen to be $dx = 28\pi/(64\sqrt{3})$ and the time step $dt = 10^{-3}$. It can be seen that the coercivity of a single crystal is larger than that of a bi-crystal.

two-grain system, comparing to the single crystal. This implies that the existence of a grain boundary facilitates the formation of the magnetic domains. This is a quite interesting result which can be also explained by consulting Eq. 10. Namely, since in the grain boundary region where $\phi = 0$, the temperature at which the ferromagnetism appears is smaller than that in the bulk. Also,

the grains are the sites of the system from which the magnetic domains start to form and grow. This affects the hysteresis curve and the coercivity of the system and the two-grain system has a smaller coercivity in comparison with the single crystal system.

B. Coercivity and grain boundary misorientation

In this section the influence of the grain boundary orientation on the coercivity is examined. Low angle boundaries are characterized by a line of dislocations separated by a distance that is inversely proportional to the misorientation angle [50], while large angle boundaries are essentially a continuous region of disorder. Typically dislocation cores lower the energy barrier for nucleation of magnetization to the lower energy state [14]. Thus the nature of the grain boundary is expected to play a key role in determining the coercivity.

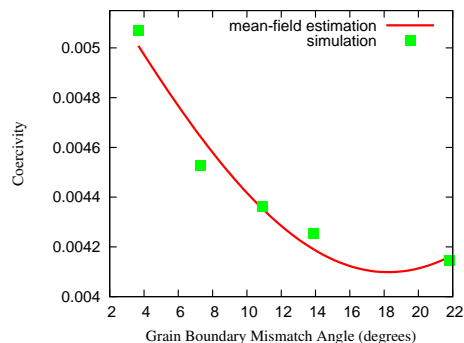


FIG. 5: The functional form $(a_1 - a_2 \sin(a_3\theta))^{3/2}$ fitted to the simulation data of the coercivity vs. the grain boundary angle for a system of $L = 256$. The fit parameters are $a_1 = 0.005$, $a_2 = 0.001$, and $a_3 = 0.08$. The coercivity decreases as we increase the grain boundary angle as predicted by the mean-field estimation.

To examine this phenomena we performed simulations by preparing a bi-crystal inside with grains that have symmetric tilt angles. The tilt angles are chosen in such a way that a perfect crystal fits inside the simulation box to prevent any change in the energy of the system regarding the boundary effects. The angles that allow perfect crystal fit inside a box of size 256×256 are $\theta = 3.67, 7.31, 10.89, 21.78$ degrees. Simulations are conducted similar the previous section.

Simulation results of the coercivity for different grain boundary angles (green pluses) are presented in Fig. 5. According to these data as the grain boundary mismatch angle increases, the coercivity of the system decreases. This is in accordance with the mean field arguments of Section IV A and the corresponding results of Fig. 4. A single-crystal system, being the limiting case of the bi-crystal system as $\theta \rightarrow 0$, has the largest coercivity comparing with the bi-crystal systems. The existence of the

grain boundary suppresses the the barrier to be overcome and a magnetic domain of opposite direction initiate from the grain boundary region.

These results and the arguments of Section IV A suggest that to approximate the coercivity in the presence of a grain boundary at a mean-field level, we replace the square of the phase amplitude ϕ^2 with $\phi^2 - NA/L$ in the magnetic free energy of the system, Eq. 7, where N is the number of dislocations per unit length of the grain boundary, A is the unit area influenced by a dislocation and L is the size of the system. Minimizing the free energy with respect to the magnetization, in the presence of an external magnetic field, \mathbf{H} , and noting that the number of dislocations in a grain boundary is related to the mismatch angle as $N \sim \sin(\theta/2)$ [50], we obtain

$$H_c = \sqrt{16B_s/(243\omega\alpha^2\phi^2 + 108\gamma B_s)} \times [(3\alpha + 6\beta)(\phi^2 - (cA/L)\sin(\theta/2)) + r_c - \beta n_0^2]^{3/2} \quad (17)$$

for the coercivity as a function of the mismatch angle θ . In this equation $c \equiv 2 \cos \delta/a$, where δ is the angle of the grain boundary with respect to the x axis and a is the lattice constant [50].

Figure 5 shows a good fit of the simulation data with the mean-field relation in Eq. 17, confirming that the model is capturing the role of grain boundary in magnetization process and coercivity.

C. Coercivity and grain size

To examine the hysteresis behavior and magnetic coercivity numerical simulations were conducted by applying an external field to bi-crystal systems of different sizes. The mean magnetization of the system as a function of the applied magnetic field for this situation is presented in Fig. 6. It can be seen that the width of the hysteresis curves change with grain size. The mean magnetization was calculated after letting the system evolve to 4×10^5 simulation time steps at each value of the \mathbf{B} field.

The coercivity extracted from the hysteresis curves is plotted in Fig. 7 as a function of grain size together with the rescaled experimental data reported in [9, 17]. The data suggest that the grain size influences the coercivity even in the absence of anisotropy. However, we obtain qualitatively different results from experiments in the limit when the grain size is much larger than the magnetic correlation length.

In our simulations, as the grain size increases, the coercivity also increases, until it reaches to a maximum value. In this regime, the grain size is smaller than the magnetic correlation length. As grain size increases in a fixed system size, the ratio of grain boundary area to grain crystalline bulk area decreases. This implies less area available for nucleation of reverse magnetization and the coercivity increases. Also, since anisotropy effect is

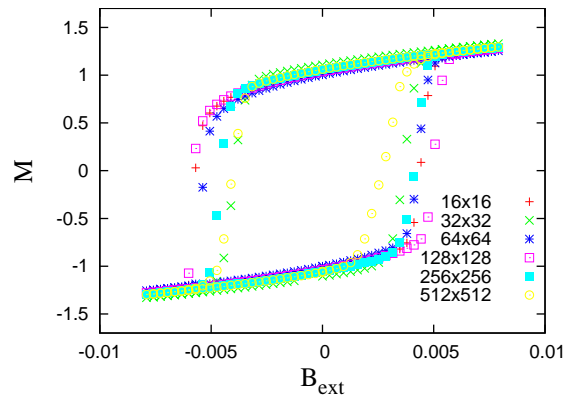


FIG. 6: Hysteresis curves for two-grain systems for different grain sizes.

not included in this model we do not expect quantitative agreement of simulation data points with experimental results for large grain size regime.

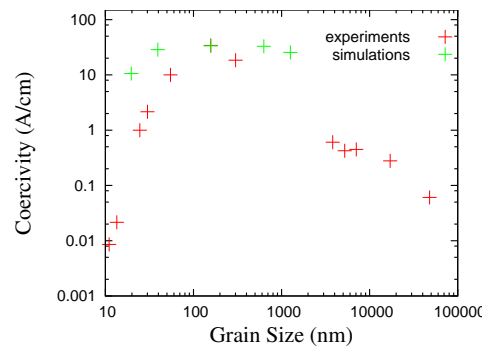


FIG. 7: Simulation coercivity data as a function of system size compared with the experimental data [19, 51]. To make the comparison more clear, the coercivity values from the simulation data are scaled by a factor of 5.5×10^3 to better compare the peak positions of both data sets.

It should be noted that in this work, the comparisons in Figs. 6 and 7 are qualitative. In the absence of magneto-crystalline anisotropy, it is expected that the coercivity will in fact tend to zero after a long enough equilibration time in the dynamics. Nevertheless, the hysteresis results reported here - essentially a meta-stable kinetic effect - point to the robustness of the model to capture some relevant features. A more quantitative examination of coercivity that includes anisotropy will be reported in an upcoming paper.

V. DISCUSSION AND CONCLUSIONS

The Landau-Lifshitz-Gilbert (LLG) equation is perhaps the most common approach to modelling the dynamics of the magnetization vector. The LLG approach and its many variants has been used to study domain walls, effect of disorder and it has been even connected to density functional theory computations [52–54], for a review see, e.g., Kurzik and Prohl [55]. In LLG, the dynamic equations are solved in a lattice but there is no direct connection with the underlying atomic structure. That is different in our approach. Here, we couple of the density field representing the atoms to the magnetic moments and our approach includes both the Curie and melting/solidification in its phase diagram. The LLG dynamics includes the precessional motion of magnetization which is important on short time scales. By Using Model A dynamics we are limiting our attention to diffusive time scales which are relevant to phase transformations. It is noted that our approach (although beyond the scope of this work), can be extended to cases such as magnetization of binary alloys and inclusion of impurities and pinning.

In summary, we extended the PFC formalism [26] to include isotropic magneto-crystalline interactions for the study of ferromagnetic solids. The advantage of this model over other phase field models of magneto-elastic systems is that it naturally incorporates atomistic features such as dislocations and grain boundaries. As a result many macroscopic properties, such as coercivity, can be linked to details of grain boundaries and polycrystalline structures. While this initial studies was for a one component two dimensional system that was magnetically isotropic it is straightforward to extend the model to include anisotropy, binary alloys and three dimensions.

VI. ACKNOWLEDGMENT

This work was supported by the Natural Science and Engineering Research Council of Canada (NSERC). We are also grateful to Compute Canada (SHARCNET and the McGill HPC Centre) for providing the computing resources. KRE acknowledges support from NSF under Grant No. DMR-0906676.

-
- [1] M. E. McHenry, M. A. Willard, and D. E. Laughlin, *Prog. Mater. Sci.* **44**, 291 (1999).
 - [2] M. E. McHenry and D. E. Laughlin, *Acta Mater.* **48**, 223 (2000).
 - [3] N. Provatas, J. A. Dantzig, B. Athreya, P. Chan, P. Stefanovic, N. Goldenfeld, and K. R. Elder, *JOM* **59**, 83 (2007).
 - [4] R. M. White, *Science* **229**, 11 (1985).
 - [5] H. Fukunaga and H. Inoue, *Jpn. J. Appl. Phys.* **31**, 1347 (1992).
 - [6] W. Rave and K. Ramstok, *J. Magn. Magn. Mater.* **171**, 69 (1997).
 - [7] R. Skomski, H. Zeng, and D. J. Sellmyer, *IEEE Trans. Magn.* **37**, 2549 (2001).
 - [8] A. Hernando and J. M. Gonzalez, *Hyperfine Interact.* **130**, 221 (2000).
 - [9] G. Herzer, in *Handbook of Magnetic Materials*, edited by K. H. J. Buschow (Elsevier Science B.V., 1997), vol. 10, chap. 3.
 - [10] J. Fidler and T. Scherfl, *J. Phys. D: Appl. Phys.* **33**, R135 (2000).
 - [11] R. Harris, M. Plischke, and M. J. Zuckermann, *Phys. Rev. Lett.* **31**, 160 (1973).
 - [12] R. Alben, J. J. Becker, and M. C. Chi, *J. Appl. Phys.* **49**, 1653 (1978).
 - [13] M. C. Chi and R. Alben, *J. Appl. Phys.* **48**, 1653 (1977).
 - [14] J. B. Goodenough, *Phys. Rev.* **95**, 917 (1954).
 - [15] A. Mager, *Ann. Physik* **6. Folge. Band 11**, 15 (1952).
 - [16] S. Flohrer and G. Herzer, *J. Magn. Magn. Mater.* **322**, 1511 (2010).
 - [17] G. Herzer, *Phys. Scr.* **T49A**, 307 (1993).
 - [18] G. Herzer, *Scripta Metall Mater* **33**, 1741 (1995).
 - [19] F. Pfeifer and C. Redeloff, *J. Magn. Magn. Mater* **19**, 190 (1980).
 - [20] R. Skomski and M. D. Coey, *Phys. Rev. B* **48**, 15812 (1993).
 - [21] R. Skomski, *Simple Models of Magnetism* (Oxford University Press, New York, 2008).
 - [22] T. Koyama and H. Onodera, *J. Phase Equilib. Diff.* **27**, 22 (2006).
 - [23] T. Koyama, *Sci. Technol. Adv. Mater.* **9**, 013006 (2008).
 - [24] J. X. Zhang and L. Q. Chen, *Acta Materialia* **2845**, 53 (2005).
 - [25] K. R. Elder, M. Katakowski, M. Haataja, and M. Grant, *Phys. Rev. Lett.* **88**, 245701 (2002).
 - [26] K. R. Elder and M. Grant, *Phys. Rev. E* **70**, 051605 (2004).
 - [27] K. R. Elder, N. Provatas, J. Berry, P. Stefanovic, and M. Grant, *Phys. Rev. B* **75**, 064107 (2007).
 - [28] P. F. Tupper and M. Grant, *Europhys. Lett.* **81**, 40007 (2008).
 - [29] A. Jaatinen, C. Achim, K. R. Elder, and T. Ala-Nissila, *Phys. Rev. E* **80**, 031602 (2009).
 - [30] A. Jaatinen and T. Ala-Nissila, *J. Phys. Condens. Matter* **22**, 205402 (2010).
 - [31] M. Greenwood, N. Provatas, and J. Rottler, *Phys. Rev. Lett.* **105**, 045702 (2010).
 - [32] M. Greenwood, J. Rottler, and N. Provatas, *Phys. Rev. E* **83**, 031601 (2011).
 - [33] J. Berry, N. Provatas, J. Rottler, and C. W. Sinclair, *Phys. Rev. B* **86**, 224112 (2012).
 - [34] V. Fallah, J. Stolle, N. Ofori-Opoku, S. Esmaili, and N. Provatas, *Phys. Rev. B* **86**, 134112 (2012).
 - [35] N. Provatas and K. Elder, *Phase Field Methods in Material Science and Engineering* (Wiley-VCH, 2010).
 - [36] P. M. Chaikin and T. C. Lubensky, *Principles of Condensed Matter Physics* (Cambridge University Press, Cambridge, 2000).

- [37] D. Herlach, C. Buhrer, D. M. Herlach, K. Maier, C. Notthoff, D. Platzek, and J. Reske, *Europhys. Lett.* **44**, 98 (1998).
- [38] D. M. Herlach, *J. Phys.: Condens. Matter* **13**, 7737 (2001).
- [39] D. Holland-Moritz, D. M. Herlach, and F. Spaepen, *Superlattice Microst.* **41**, 196 (2003).
- [40] W. F. Brown, in *Handbook of Physics*, edited by E. U. Condon and H. Odishaw (McGraw-Hill, New York, 1958), chap. 8.
- [41] J. D. Jackson, *Classical Electrodynamics* (John Wiley and Sons Inc., New York, 1998).
- [42] N. Goldenfeld, B. P. Athreya, and J. A. Dantzig, *Phys. Rev. E* **72**, 020601 (2005).
- [43] B. P. Athreya, N. Goldenfeld, and J. A. Dantzig, *Phys. Rev. E* **74**, 011601 (2006).
- [44] P. Y. Chan and N. Goldenfeld, *Phys. Rev. E* **80**, 065105 (2009).
- [45] K. R. Elder, Z.-F. Huang, and N. Provatas, *Phys. Rev. E* **81**, 011602 (2012).
- [46] L. D. Landau, E. M. Lifshitz, and L. P. Pitaevskii, *Electrodynamics of Continuous Media*, vol. 8 (Elsevier Pte Ltd., Singapore, 2007).
- [47] R. Atkin and N. Fox, *An Introduction to the Theory of Elasticity* (Longman, New York, 1980).
- [48] P. C. Hohenberg and B. I. Halperin, *Rev. Mod. Phys.* **49**, 435 (1977).
- [49] M. Patra and M. Karttunen, *Num. Meth. Part. Diff. Eqs* **22**, 936 (2005).
- [50] W. T. Read and W. Shockley, *Phys. Rev.* **78**, 275 (1950).
- [51] G. Herzer, *IEEE Trans. Magn.* **26**, 1397 (1990).
- [52] J. Iwasaki, M. Masahito Mochizuki, and N. Nagaosa, *Nature Comms.* **4**, 1463 (2013).
- [53] R. Chimata, A. Bergman, L. Bergqvist, B. Sanyal, and O. Eriksson, *Phys. Rev. Lett.* **109**, 157201 (2012).
- [54] T. Fal, M. Plumer, J. Whithead, J. Mercer, J. van Ek, and K. Srinivasan, *Appl. Phys. Lett.* **102**, 202404 (2013).
- [55] M. Kruzik and A. Prohl, *SIAM Rev.* **48**, 439 (2006).